HHS Public Access

Author manuscript

J Fluids Eng. Author manuscript; available in PMC 2022 June 06.

Published in final edited form as:

J Fluids Eng. 2022 June ; 144(6): . doi:10.1115/1.4054099.

Numerical Investigation of Aerosolization in the Venturi Dustiness Tester: Aerodynamics of a Particle on a Hill

Nithin Kumar Palakurthi, **Urmila Ghia**

Mechanical and Materials Engineering, College of Engineering and Applied Science, University of Cincinnati, Cincinnati, Ohio 45221-0072

Leonid A. Turkevich*

Engineering and Physical Hazards Branch (EPHB), Division of Field Studies and Engineering (DFSE), National Institute for Occupational Safety and Health (NIOSH), Centers for Disease Control and Prevention (CDC), 1090 Tusculum Avenue, Cincinnati, Ohio 45226

Abstract

Understanding particle detachment from surfaces is necessary to better characterize dust generation and entrainment. Previous work has studied the detachment of particles from flat surfaces. The present work generalizes this to investigate the aerodynamics of a particle attached to various locations on a model hill. The present work serves as a model for dust aerosolization in a tube, as powder is injected into the Venturi Dustiness Tester. The particle is represented as a sphere in a parallel plate channel, or, in two dimensions, as a cylinder oriented perpendicular to the flow. The substrate is modified to include a conical hill (3D) or wedge (2D), and the test particle is located at various positions on this hill. The governing incompressible Navier-Stokes equations are solved using the finite-volume FLUENT code. The coefficients of lift and drag are compared with the results on the flat substrate. Enhanced drag and significantly enhanced lift are observed as the test particle is situated near the summit of the hill.

Keywords

Drag; Lift; Aerosolization; Dustiness; Computational Fluid Dynamics

*Corresponding Author: LLT0@cdc.gov, Tel.: 513.841.4518.

Dedication

This paper reports research contained in the thesis of Palakurthi [9], which was the last thesis defense that Professor Kirti Ghia adjudicated. We recall his acute yet generous constructive criticism which enhanced the quality of that thesis. We dedicate this paper to his memory.

1. Introduction

1.1 Introduction

Aerosolization of particles from surfaces [1] is of particular interest to the study of the dustiness of powders [2–3]. Natural examples of this phenomenon are pollen grains or dust suspended in air, and sand particles carried away by the wind [4–7]. Airborne organic (*e.g.*, soot, pollens, molds, bacteria, virus) and inorganic (*e.g.*, silica, asbestos) dust may adversely affect health. Successful delivery of powdered pharmaceuticals presupposes efficient aerosolization of the powder [8]. Previous work [9–10] studied aerodynamics of particles located on flat surfaces.

The National Institute for Occupational Safety and Health (NIOSH) has a comprehensive program to study the dustiness of powders [2–3]. NIOSH and other laboratories [11] extensively utilize the Venturi Dustiness Tester (VDT) [12], which permits dustiness measurement at high Reynolds number of small quantities of expensive or potentially dangerous powders (e.g. pharmaceuticals, nanoparticles). In the VDT configuration [13], a small quantity (mg) of powder is placed in a slender tube; a high velocity air stream is forced through the tube and over the powder hill; individual particles are lifted from the powder hill and are aerosolized; the aerosol is swept into a containment chamber where it is then sampled. Dubey *et al* [13] modeled the air flows in the VDT, assuming the aerosolization process to have already taken place. The current work addresses the aerosolization process itself, i.e. the lift and drag of particles from the powder hill. Our numerical approach is restricted to flow in the laminar regime. Sharma *et al.* [14–15] have extended this work to higher Re, where the dynamics of vortex shedding from the hill becomes important.

1.2 Literature Review

Many factors contribute to the detachment of particles from surfaces [16]. When a fully developed laminar boundary layer flows parallel to a substrate, the shear flow at the surface generates aerodynamic forces and moments. For the particle to detach, these aerodynamic forces must exceed the surface (*e.g.*, capillary, adhesion) or body (*e.g.*, gravity, van der Waals) forces which hold the particle onto the surface. The experimental measurement of these forces on isolated particles is challenging [17–24]. Numerical modeling is appropriate to study such problems.

For fine and ultrafine particles (micron and nanometer diameter), the particle Reynolds number (based on the local flow velocity and particle radius) is typically less than unity. The Stokes drag (creeping flow) for a sphere in a uniform steady incompressible flow in the absence of any wall is $F_{drag} = 3\ \pi\ \mu\ u\ D$, where u is the uniform free-stream flow velocity, D is the sphere diameter, and μ is the fluid viscosity. $F_{lift} = 0$. O'Neill [25] found that the presence of a wall increases the drag by a factor f = 1.7009. Leighton & Acrivos [26] included the first inertial correction to creeping flow and found $F_{lift}/F_{drag} = 0.287$ Re. This differs from the earlier Saffman [27] result, also a lowest inertial correction to creeping flow, valid for large shear flow and no wall; the corresponding 2D analog, namely, of a cylinder in linear shear flow, was studied by Bretherton [28]. Cherukat *et al* [29] discuss the cross-over between the Saffman and Leighton-Acrivos regimes. The effect of a finite gap

between particle and wall for $2 < Re < 250$ has been studied [30–32]. Lee & Balachandar [33] studied the modification of lift and drag due to motion of the particle parallel to the boundary. The Finlay group [34–36] examined the related problem of a sphere or cylinder attached to a wall in a Blasius boundary layer, where additional lift derives from the vertical velocity near the plate as the boundary layer develops.

Multiple laminar experiments have been conducted [37–43]. The larger lift on an attached particle in a turbulent boundary layer has been studied [44–45]. The importance of aerodynamic forces on the migration and resuspension of small particles has been extensively studied [46–57].

The primary focus of the earlier studies has been an understanding of the wall-induced forces on a particle. More relevant for the VDT [2, 12–13] is a particle of a finely divided solid (a powder) situated in proximity to a collection of other similar particles, namely on a powder hill. The aerodynamics of a particle when it is located on a hill has not previously been studied.

In the VDT, powder is pre-loaded at the base of a ‘tee’-shaped tube (Figure 1) which is open to the atmosphere (at top and right) and which is inserted (towards the left) into a cubical dustiness sampling chamber. In a short ($\Delta t = 1.5$ sec) dispersion phase, the pressure in the dustiness chamber is lowered, and an air stream is induced to flow over the powder hill. This air stream ($Re \sim 2 \times 10^4$) aerosolizes the powder particles from the hill, and the resulting aerosol enters the dustiness chamber (at left) as a jet. The earlier modeling study of the VDT [13] presupposed aerosolization—it considered an aerosol stream entering the dustiness chamber as a jet. In the present work, we address the aerosolization process itself.

As discussed later, in Section 2.2, the air flow in the VDT tube is turbulent ($Re_{tube} \sim 2 \times 10^4$). At these air flows, we expect vortices to be shed from the powder hill obstruction [58–62]; this is seen in the work of Sharma *et al.* [14–15]. Vortex shedding is suppressed due to the confined geometry [63–66]. Additional complications arise due to the porosity of the obstruction [67] and due to the dynamic disappearance of the obstacle (as particles are aerosolized from the hill). In the current, over-simplified, study, we restrict this investigation to low air flows ($Re_{sphere} < 10^2$) so that the flows may be treated as steady-state. We seek to understand whether the usual drag and lift of the powder particle are significantly altered from their planar values due to the obstruction geometry. In particular, we seek to determine whether it is any easier to aerosolize a particle from the hill than from a flat surface.

It is important to determine if the lift and drag forces, which contribute to the particle detachment process, and the torque, which determines the particle rotation upon detachment, are modified for a nonplanar substrate. Hence, the present study considers flow over a particle attached to a hill and compares it to the idealized case of the isolated particle attached to the plane wall. This is not a true many-body study but represents a first attempt to take into account the effect of a nonplanar substrate on particle aerosolization. We note that effects of a nonplanar substrate will be important for any treatment of particle detachment from rough surfaces, which, at the microscopic scale, consist of protuberances

and valleys. Length limitations restrict the discussion in this paper to lift and drag; our simulation results for torque are contained in [9].

1.3 Outline of this Paper

This paper is organized as follows. Section 1 introduces dustiness, the Venturi Dustiness Tester (VDT), which motivates the problem of aerosolization of particles from a hill. Section 2 discusses the mathematical formulation underlying our simulations. We also discuss (Section 2.1.2) the peculiar geometry of a curved surface in contact with a flat surface, which necessitates displacing the particle slightly above the substrate. Grid refinement is discussed in Section 2.1.6. Conditions for the relevance of our simulations to the VDT are presented in Section 2.2. Section presents the results of these simulations: 2D (cylinder on a wedge) in Section 3.1 and 3D (sphere on a cone) in Section 3.4. A major result of our study is that the aerodynamic lift on the particle is significantly enhanced at the summit of the hill. The origin of this effect is discussed in Section 3.3 and further in the Supplemental Material (Section S4). Section 4 presents our conclusions and recommendations for further work on this problem.

2. Mathematical Formulation and Numerical Modeling

2.1 Numerical Modeling

This work studies the aerodynamic lift and drag forces on a particle positioned on a conical hill and slightly elevated above the hill surface. The particle is approximated as a sphere (in 3D) or as a cylinder (in 2D), with the cylinder orientated perpendicular to the free-stream direction. All the simulations are performed in the laminar regime $1 < Re_{channel} < 2000$, corresponding to $0.07 < Re_{hill} < 133$ and to $0.01 < Re_{cyl/sph} < 13$. We assume incompressible, steady flow, and we neglect the effects of additional surface and body forces. The parameters of STP air are density $\rho = 1.225$ kg/m^3 and dynamic viscosity $\mu = 1.78 \times 10^{-5}$ kg/m-sec; lengths are measured in mm.

2.1.1 Governing Equations—

Conservation of the mass is given by

$$\frac{\partial \rho}{\partial t} + \frac{\partial \rho u_i}{\partial x_i} = 0 \tag{3.1}$$

where u_i is the fluid velocity.

Conservation of momentum is given by

$$\frac{\partial \rho u_i}{\partial t} + \frac{\partial (u_j \rho u_i)}{\partial x_j} - \frac{\partial \tau_{ij}}{\partial x_j} + \frac{\partial \rho}{\partial x_i} = 0 \tag{3.2}$$

where p is the static pressure; the stress tensor, τ, is given by

$$\tau_{ij} = \mu\left(\frac{\partial u_i}{\partial x_j} + \frac{\partial u_j}{\partial x_i} - \frac{2}{3}\frac{\partial u_k}{\partial x_k}\delta_{ij}\right) \tag{3.3}$$

2.1.2 Geometry

2.1.2.1 Elevated versus Embedded Particle: Placing the particle in contact with the plane wall introduces a singular point at the contact point. This is numerically challenging for grid generation [35]. Because of this singular point, an improperly constructed grid may contain poor quality cells (high skewness, poor orthogonality, high aspect ratios). Potential solutions to this problem are to either slightly elevate the particle above the surface or slightly embed the particle into the surface. A brief discussion of this problem is provided in the Supplemental Material (Section S1 for 2D and Section S2 for 3D). In the current study, we have taken the approach to elevate the test particle slightly above the wedge/conical substrate (perpendicular distance to the cylinder/sphere center x/R = 1.05).

2.1.2.2 Two-Dimensional Study – Flow over a Cylinder on a Wedge in a Channel: A cylinder, oriented perpendicular to the flow, is positioned (Figure 2) at different locations, θ, on a wedge submerged in a laminar fully developed flow. The diameter of the cylinder is D; the wedge height is L. The channel height is 15L (so there is minimal constriction of the flow by the wedge), and the inlet/outlet boundaries are placed 15L/20L upstream/downstream, respectively, of the wedge center.

We have performed flow simulations and determined the lift, drag and torque for the following cases: a) 3 cylinder diameters, D = 2 mm, 1 mm and 0.5 mm, at fixed particle location, θ, wedge half-angle, α, and height, L; b) 3 wedge heights, L = 6.5 mm, 13 mm and 19 mm, at fixed cylinder diameter, D, particle location, θ, and wedge half-angle, α; c) 3 wedge half-angles, α = 30°, 45° and 60°, at fixed cylinder diameter D, wedge height, L, and particle location, θ.

2.1.2.3 Three-Dimensional Study – Flow over a Sphere on a Cone in a Channel: A sphere is positioned at different locations on a cone, submerged in a laminar, fully developed flow. The boundaries are placed as in the 2D case (Section 2.1.2.2) so that the upstream effects of the cone and sphere have minimal effects on the solution. The lift and drag forces and torque acting on the sphere are computed for various locations of the sphere positioned axially (θ) on and azimuthally (φ) around the cone (the latter at fixed θ).

2.1.3 Solver—The commercial code used in this study is Ansys FLUENT v.16, which employs a finite-volume method, where the conservation laws are used in their integral form. The incompressible continuity and momentum equations are solved by the SIMPLE (Semi-Implicit Method for Pressure-Linked Equations) algorithm, which iteratively solves for the coupled velocity and pressure fields [68]. The residual for the convergence criterion was set at 10^{-6}. The second-order accurate implicit upwind and second-order implicit central difference schemes are used to discretize the convection and diffusion terms respectively.

2.1.4 Boundary Conditions

- No Slip boundary at the particle surface, on top and bottom plates, and on the surface of the wedge/cone.
- Slip boundary on the side walls.

- Fully developed parabolic velocity profile is initialized at the channel inlet.
- Pressure boundary condition (set to atmospheric pressure) at the channel outlet.

2.1.5 Mesh Generation—Ansys Mesh Modular is used to generate structured grids for the flow geometries considered. Care has been taken to resolve wall normal velocity gradients in the boundary layer on the no-slip surfaces.

2.1.6 Grid Refinement Study

2.1.6.1 2D Grid Refinement--Cylinder on a Wedge: A detailed grid refinement analysis [69] is carried out on successively refined grids to estimate the error in the numerical results due to the discretization. The grid refinement study is constructed for the case with cylinder diameter D = 2 mm; wedge height L = 13 mm; wedge half-angle $\alpha = 60°$; the cylinder is located at $\theta = 60°$ on the wedge. The area of the domain is $A = 8.1737 \times 10^4$ mm^2. The refinement ratio is 1.5. For the medium grid, there are 36 cells around the cylinder and 6 cells in the gap. The absolute drag and lift forces (not normalized to their upstream values) acting on the cylinder are computed for successive grids, and the percent changes are presented in Table 1. As the changes in these forces with mesh refinement are less than 1%, the coarsest grid was used for the reported parametric study.

2.1.6.2 3D Grid Refinement--Sphere on a Cone: A detailed grid refinement analysis [69] is carried out on successively refined grids to estimate the error in the numerical results due to the discretization. Sphere diameter D = 2 mm; cone height L = 13 mm; cone half-angle $\alpha = 60°$; the sphere is located at $\theta = 80°$ on the cone. The volume of the domain is $V = 1.5375 \times 10^7$ mm^3. Two refinements are studied: r = 1.27 (for the coarse-to-medium grid refinement); r = 1.58 (for the medium-to-fine grid refinement). For the medium grid, there are 36 cells around the sphere and 6 cells in the gap. The absolute drag and lift forces (not normalized to their upstream values) acting on the sphere are computed for these successively refined grids, and the percent changes are presented in Table 2. As the changes in these forces with mesh refinement are less than 1%, the coarsest grid was used for the reported studies.

2.2 Comment on the Applicability of these Simulations to Powder Aerosolization in the VDT

The diameter of the VDT inlet nozzle is $D_{tube} = 0.44$ cm. During injection, the volumetric flow rate, Q = 60.0 L/min, corresponds to an average flow velocity $u_{av} \sim 65.8$ m/s and Reynolds number $Re_{tube} \sim 19{,}900$. While this is clearly turbulent flow throughout the bulk of the nozzle, a particle near the wall (*i.e.*, within the viscous sublayer), experiences a much slower flow. Using a flow profile $u \sim u_{max} (1 - r/R)^{1/n}$, with $n \sim 6$ (appropriate for $Re \sim 19{,}900$), $u_{max}/u_{av} = (n+1)(2n+1)/2n^2$, whence $u_{max} \sim 83.2$ m/sec. For a $d \sim 1$ μm particle resting on the tube surface, the velocity experienced at its center is $u_{particle} \sim u_{max} (d/D)^{1/n} \sim 23.1$ m/sec. The ratio of particle to tube Reynolds numbers is $Re_{particle}/Re_{tube} = (u_{particle}/u_{av})*(d/D) \sim 8 \times 10^{-5}$, whence $Re_{particle} \sim 1.6$. Modeling the drag, lift and torque with a local laminar flow is thus a reasonable first approach to this problem.

3. Simulation Results and Discussion

3.1 2D Flow over a Cylinder on a Wedge

The cylinder (D = 2 mm) is positioned at various locations, θ, on the wedge (L = 13 mm, wedge half-angle α = 30°), as discussed in section 2.1.2.2. Simulations are conducted for channel Reynolds numbers $Re_{channel} < 1920$, for which the flow remains laminar, consistent with pipe flow transition at $Re_c \sim 2300$ [70].

Figure 3a displays the normalized drag, $F_{drag}(\theta)/F_{drag}(0)$, and Figure 4a displays the normalized lift $F_{lift}(\theta)/F_{lift}(0)$ normalized by their upstream values (*i.e.* at θ = 0).

The normalized drag increases as the cylinder is located higher up on the wedge, attaining a maximum drag just upstream of the wedge apex (θ ~ 90°). For 120° < θ < 150°, the cylinder is 'shielded' by the wedge and experiences no drag. The maximum normalized drag is in the range 5 – 7.5.

On the other hand, the normalized lift varies dramatically. As the test cylinder is positioned at the various locations, θ, on the wedge surface, the normalized lift increases as the test cylinder moves up the upstream side of the wedge, reaching a maximum at θ ~ 80°, and then decreases on the downstream side of the wedge; there is an 'undershoot' (the lift is minimum and even negative for θ ~ 100°) and then a 'rebound' as the lift increases further downstream of the wedge. The enhancement effect is not small (in the range 8 to 19) and increases with increasing Re. The undershoot effect is similarly not small (in the range −5 to −16) but decreases in magnitude with increasing Re. Recall that a negative lift means that the airflow actually presses the test particle against the surface.

The maximum normalized lift is 3–4 times larger than the maximum normalized drag. Finally, while the lift experiences an 'undershoot' (negative lift at θ ~ 100°), the normalized drag exhibits no such anomaly.

3.2 Wedge Angle Dependence

We now discuss the effect of varying the wedge half-angle, α. The effects of varying the wedge height, L, and the cylinder diameter, D, are discussed in the Supplemental Material (Section S3). For the wedge height study, the normalized drag (Figure S5) and normalized lift (Figure S6) are plotted as a function of channel Re.

Figures 3 and 4 present results for two additional wedge half-angles α = 45° and 60°, also at D = 2 mm and L = 13 mm. Both the normalized lift and drag appear to be relatively insensitive to the magnitude of the wedge half-angle, α. The increase in normalized drag, as the test cylinder is positioned at higher locations on the wedge, is preserved for these sharper wedges (Figure 3). The general structure in the normalized lift (maximum lift at θ ~ 80°, with minimum, negative lift at θ ~ 100°) is preserved (Figure 4).

3.3 Origin of the Enhanced Drag and Lift

The origin of the enhanced drag and lift forces, as the cylinder is positioned at different locations on the wedge, is examined in the Supplemental Material (Section S4), for the case

of Re = 1. Both forces result from cancelations in the pressure and shear contributions from different regions of the cylinder surface; these cancellations become less complete at higher elevations on the wedge.

Figure 5 shows that the variation in the normalized drag closely follows the variation in the normalized velocity parallel to the substrate. Similarly, the variation in the normalized lift closely follows the variation in the normalized velocity normal to the substrate (Figure 6). While the normalized drag is amplified over the normalized parallel velocity (the dotted line is above the solid line in Figure 5), the normalized lift is suppressed below the normalized perpendicular velocity (the dotted line is below the solid line in Figure 6).

When the fully developed flow encounters the wedge base, a new boundary layer begins to develop as the flow turns up the wedge; the incompressible fluid is accelerated (flow constriction), with a concomitant upward vertical acceleration. Similarly, when the newly established fully developed flow (going up the wedge) encounters the apex of the wedge (flow expansion), the flow is decelerated, with a concomitant downward vertical acceleration.

3.4 3D Flow over a Sphere on a Cone

The flat substrate is augmented by a cone, with half-angle $\alpha = 60°$; the simulation flow remains laminar for $Re_{channel} < 1920$, consistent with pipe transition to turbulence at $Re_c \sim 2300$ [70]. Figures 7 and 8 display the normalized drag and lift, where these are normalized using the lift and drag forces experienced by the sphere at $\theta = 0°$.

The normalized drag profile (Figure 7) for the flow over a sphere on the cone, as function of location θ, is very similar to the 2D results (Figure 3a). As in 2D, maximal drag is observed at $\theta = 80°$ for all Reynolds numbers. The drag increases as the sphere is moved from the bottom to the peak on the upstream side of the cone and then decreases gradually to minimal drag in the 'sheltered' location downstream ($\theta = 180°$). For $Re_{channel} = 1920$, the maximum normalized drag is 4.5, which is smaller than the maximum normalized drag (7.4) in the 2D simulations.

The normalized lift profile (Figure 8) for the sphere placed on the cone is similar to the 2D results (Figure 4a). A maximum normalized lift occurs ($\theta = 80°$) for the sphere on the upstream side of the cone apex; a minimum negative lift occurs for the sphere located on the downstream side of the cone ($\theta = 100°$). This suggests that the sphere located near the top of the cone can be more easily lifted by the fluid, compared to the identical sphere located near the bottom of the cone. The variation in normalized lift is considerably larger in 3D than in 2D, *e.g.*, maximum normalized lift (for Re = 1920) is 104 in 3D but only 28 in 2D.

The behavior near the summit ($\theta = 80°, 100°$) is examined as a function of channel Re. The normalized drag is shown in Figure 9; the normalized drag is shown in Figure 10. In both cases, the Re-variation is less pronounced than the variation with location on the hill.

3.5 Azimuthal Variation

We have also studied the azimuthal variation of the lift and drag forces on the sphere; we considered 6 azimuthal angles, φ, circumambulating the cone at $\theta = 60°$

Results for the normalized drag for flow over a sphere on a cone as function of azimuthal angle, φ, at $\theta = 60°$, are plotted in Figure 11. The reference drag used for normalization is the drag experienced by the sphere located at $\theta = 0°$. There is only gradual variation in the normalized drag as the sphere moves azimuthally around the cone, with variation in the range 2.4 – 3.9

We have also studied the behavior of the normalized lift for the flow over a sphere placed at various azimuthal angles around the cone for $\theta = 60°$ (Figure 12). The maximum lift occurs for the sphere on the upstream side of the cone ($\varphi = 0°$), and the minimum occurs for the sphere located on the downstream side of the cone ($\varphi = 180°$). The normalized lift varies significantly when compared to the variations in the normalized drag. The net upwards force experienced by the sphere decreases as the sphere is moved azimuthally around the cone. This suggests that a particle located on the upstream side of the hill is more easily lifted by the fluid, compared to a similar particle located at other azimuthal positions on the hill.

3.6 Enhanced Particle Detachment from the Hill Summit

In order for the air flow to detach a particle from a flat surface, or from a hill, the aerodynamic lift force must exceed any adhesive forces (which considerably exceed the gravitational weight for fine and ultrafine particles). Measurement of particle adhesive forces is notoriously difficult, and the literature is extensive. For the following discussion, we consider two elegant experiments: i) use of an atomic force microscope tip to effect detachment [71]; ii) detaching small particles via a Huntington bar shock pulse [72]. We look for data relevant to our simulations of silica particles.

Jones *et al.* [71] measured the adhesive force of three relevant systems: i) small glass sphere ($r = 20$ μm) on the following flat plates: (a) hydrophilic glass: $4\ \mu N < F_{adh} < 7\ \mu N$; (b) hydrophilic Si: $4\ \mu N < F_{adh} < 9\ \mu N$; ii) large glass sphere ($r = 100$ μm) on hydrophilic glass: $0.5\ \mu N < F_{adh} < 2\ \mu N$. The ranges were the result of variations in the relative humidity. Wanka *et al.* [72] measured the adhesive force for silica spheres on a hydrophilic-treated polystyrene substrate: i) $d = 4$ μm: $F_{adh} = 70$ nN; ii) $d = 10$ μm: $F_{adh} = 150$ nN.

The aerodynamic lift force is given by $F_{lift} = C_{lift} * (1/2\ \rho\ u^2) * \pi D^2$. The particle velocity is given by $u = Re_{sphere}\ \nu/D$, whence $F_{lift} = (\pi/2) * C_{lift} * \rho \nu^2\ Res_{phere}^2 = 0.42$ nN Res_{phere}^2, using the density and kinematic viscosity of air.

Aerodynamic detachment from a flat surface should occur for the AFM system for the ranges: i) small glass (20 μm): (a) hydrophilic glass: $100 < Re_{sphere} < 130$; hydrophilic Si: $100 < Re_{sphere} < 150$; ii) large glass (100 μm) from hydrophilic glass: $35 < Re_{sphere} < 70$. Similarly, aerodynamic detachment from a flat surface should occur for the Huntington shock systems: i) 4 μm silica: $Re_{sphere} \sim 13$; 10 μm silica: $Re_{sphere} \sim 19$. Recall (section 2.2) that a micron sized particle in the boundary layer of a flat surface (using the VDT flow conditions) experiences $Re_{sphere} \sim 2$, which would seem to be insufficient to detach the

particles. However, for a particle at the summit of a hill, the aerodynamic lift is enhanced by a factor of 10^2; the required detachment Re_{sphere} decreases by a factor of 10, which is then of the right order of magnitude for the VDT to effect detachment.

4. Conclusions

4.1 Conclusions

In this work, we studied the variation in aerodynamic forces (lift and drag) on a test particle placed at various positions on a hill (2D--cylinder located on a wedge; 3D--sphere located on a cone). We have studied variations in lift and drag due to position on the hill (θ location), Reynolds number of the flow, and geometry of the hill (cone/wedge half-angle α); in 3D there is also azimuthal variation.

In the geometric models for the hill, the cylinder and sphere were minimally offset above the substrate, with the offset (measured normally from the particle center) required to obviate the otherwise encountered geometric singularity at the contact point. The incoming flow considered is steady laminar fully developed flow. The aerodynamic forces computed for each location (θ position) are normalized using the forces experienced by the particle upstream of the hill (*i.e.*, at θ = 0°). In both 2D and 3D, the lift force experienced by the particle, near the peak of the hill upstream (wedge or cone), is greater than the force experienced by the particle on the planar substrate. This suggests that particles located upstream and near the peak of the obstacle tend to be lifted more easily.

A detailed parametric study was performed for different wedge angles, heights and cylinder diameters. The results suggest that, as the cylinder diameter decreases, the normalized lift increases, whereas the normalized drag is relatively insensitive to cylinder size. The normalized lift and drag both increase with wedge height. In 3D, forces are also computed for the sphere at azimuthal locations around the cone.

4.2 Recommendations for Future Work

An immediate extension of this work would be to modify the structure of the substrate to model a rough surface, which consists, at the microscopic scale, of hills and valleys. The dislodgement of particles from the rough surface (lift and drag) can then be modeled, taking into account the variation in lift and drag for the test particle situated upstream or downstream of the protuberance. Cheng *et al.* [73] have reported that a significant roughness reduces the normal pull-off force to a fraction of its smooth-surface value.

Any quantitative evaluation of particle detachment must take into account the physicochemical forces (surface, van der Waals and electrostatic) between the particle and the surface. Extensive reviews of adhesion forces are available in [18, 20]. Microparticles must overcome adhesion forces in order to detach from a surface. The adhesion force acting on the particle surface is distributed based on the surface irregularities present on the particle surface and its contacting surface. Particle shape and composition may be more important than the size, owing to their effect on the adhesion force [74].

The present work has been limited to steady laminar flow conditions. Sharma *et al.* [14–15] have extended these results to the turbulent regime.

Finally, the powder hill has been modeled as a monolithic cone or wedge. A realistic powder hill has nonzero porosity and permeability and might be better modeled using Darcy flow through the hill.

Supplementary Material

Refer to Web version on PubMed Central for supplementary material.

Acknowledgments

We thank J. Bennett, K.H. Dunn and D.E. Evans (all of NIOSH) for helpful discussions and for a careful reading of the manuscript. This work was supported in part by the NIOSH Nanotechnology Research Center.

References

[1]. Fuchs NA (1964). The Mechanics of Aerosols (Oxford: Pergamon), chapter 8.

[2]. Evans DE, Turkevich LA, Roettgers CT, Deye GJ, Baron PA (2013). Dustiness of Fine and Nanoscale Powders, Ann. Occup. Hyg 57: 261. [PubMed: 23065675]

[3]. Evans DE, Turkevich LA, Roettgers CT, Deye GJ (2014). Comment on comparison of powder dustiness methods Ann. Occup. Hyg 58: 524–528. [PubMed: 24477891]

[4]. Bagnold RA (1954). The Physics of Blown Sand and Desert Dunes (London: Methuen).

[5]. Andreotti B, Claudin P, Pouliquen O (2006). Aeolian sand ripples: experimental study of fully developed states. Phys. Rev. Lett 96: 02801.

[6]. Duran O, Claudin P, Andreotti B (2014). Direct simulation of Aeolian sand ripples. PNAS 111: 15665–15668. [PubMed: 25331873]

[7]. Cheng H, Liu C, Li J, Liu B, Zheng Z, Zou X, Kang L, Fang Y (2017). Experimental study of Aeolian sand ripples in a wind tunnel. Earth Surface Process. Landforms doi: 10.1002/esp.4246.

[8]. Finlay WH (2001). The Mechanics of Inhaled Pharmaceutical Aerosols: An Introduction (San Diego: Academic).

[9]. Palakurthi NK (2017). Aerodynamics of Particle Detachment from Surfaces: A Numerical Study, M.Sc. thesis, Univ. Cincinnati, Engineering & Applied Sciences, Mechanical Engineering.

[10]. Palakurthi NK, Ghia U, Turkevich LA (2017). Simulations of Particle Detachment from a Flat Surface. Proceedings of the ASME 2017 Fluids Engineering Division Summer Meeting FEDSM 2017–69111.

[11]. Bach S, Eickmann U, Schmidt E (2013). Comparison of established systems for measuring the dustiness of powders with the UNC Dustiness Tester developed especially for pharmaceutical substances. Ann. Occup. Hyg 57: 1078–1086. [PubMed: 23749502]

[12]. Boundy M, Leith D, Polton T (2006). Method to evaluate the dustiness of pharmaceutical powders. Ann. Occup. Hyg 50: 453–458. [PubMed: 16484334]

[13]. Dubey P, Ghia U, Turkevich LA (2017). Computational fluid dynamics analysis of the Venturi Dustiness Tester. Powder Technology 312: 310–320. [PubMed: 28638167]

[14]. Sharma A, Ghia U, Turkevich LA (2020). Effects of vortex shedding on the aerosolization of a particle from a hill using Large Eddy Simulation. Proceedings of the 2020 AIAA Aviation Forum, paper 539120.

[15]. Sharma A, Ghia U, Turkevich LA (2020). Large Eddy Simulation of flow over a hemispherical obstacle within a circular tube. Proceedings of the ASME 2020 Fluids Engineering Division Science Meeting FEDSM2020, paper 10596.

[16]. Sharma MM, Chamoun H, Sarma DSR, Schechter RS (1992). Factors controlling the hydrodynamic detachment of particles from surfaces. J. Coll. Int. Sci, 149: 121–134.

[17]. Bowling RA (1985). An analysis of particle adhesion on semiconductor surfaces. J. Electrochem. Soc, 132: 2208–2214.

[18]. Bowling RA (1988). A theoretical review of particle adhesion in *Particles on Surfaces 1: Detection, Adhesion, Removal* ed. by Mittal KL (Boston: Springer), pages 129–142.

[19]. Willetts BB & Naddeh KF (1986). Measurements of lift on spheres fixed in low Reynolds number flows. J. Hydraulic Res 24: 425–435.

[20]. Ranade MB (1987). Adhesion and removal of fine particles on surfaces. Aerosol Sci. Tech, 7: 161–176.

[21]. Yiantsios SG & Karabelas AJ (1995). Detachment of spherical microparticles adhering on flat surfaces by hydrodynamic forces. J. Coll. Int. Sci, 176: 74–85.

[22]. Hatakentaka K, Tanaka K, Fuchiwaki M, Shimizu F (2003). Drag and Lift Acting on a Circular Cylinder in Laminar Boundary Layer: Part 1—Verification of Force Transducer for Measuring Small Force. In ASME/JSME 2003 4th Joint Fluids Summer Engineering Conference (pp. 1147–1153). American Society of Mechanical Engineers.

[23]. Essawey AHI (2004). Microparticle detachment from surfaces by fluid flow (Doctoral dissertation, University of Notre Dame).

[24]. Ibrahim AH, Dunn PF, Qazi MF (2008). Experiments and validation of a model for microparticle detachment from a surface by turbulent air flow. J. Aerosol Sci, 39: 645–656.

[25]. O'Neill ME (1968). A sphere in contact with a plane wall in a slow linear shear flow. Chem. Eng. Sci, 23: 1293–1298.

[26]. Leighton D & Acrivos A (1985). The lift on a small sphere touching a plane in the presence of a simple shear flow. Z. Angew. Math. Phys, 36: 174–178.

[27]. Saffman PGT (1965). The lift on a small sphere in a slow shear flow. J. Fluid Mech, 22: 385–400; (corrigendum) *31*: 624 (1968).

[28]. Bretherton FP (1962). Slow viscous motion round a cylinder in simple shear. J. Fluid Mech 12: 591–613.

[29]. Cherukat P, McLaughlin JB, Dandy DS (1999). A computational study of the inertial lift on a sphere in a linear shear flow field. Int. J. Multiphase Flow, 25: 15–33.

[30]. Cherukat P & McLaughlin JB (1993). The inertial lift on a rigid sphere in a linear shear flow field near a flat wall. J. Fluid Mech 263: 1–18.

[31]. Cherukat P, McLaughlin JB, Graham AL (1994). The inertial lift on a rigid sphere translating in a linear shear flow field. Int. J. Multiphase Flow 20: 339–353.

[32]. Zeng L, Najjar F, Balachandar S, Fischer P (2009). Forces on a finite-sized particle located close to a wall in a linear shear flow. Phys. Fluids, 21: 033302.

[33]. Lee H & Balachandar S (2010). Drag and lift forces on a spherical particle moving on a wall in a shear flow at finite Re. J. Fluid Mech, 657, 89–125.

[34]. Sweeney LG (2006). Blasius Boundary Layer Flow over a Cylinder and Sphere Attached to a Wall: Characterization of Lift and Drag Forces. M.Sc. thesis, Univ. Alberta.

[35]. Sweeney LG & Finlay WH (2007). Lift and drag forces on a sphere attached to a wall in a Blasius boundary layer. J. Aerosol Sci, 38: 131–135.

[36]. Martinez RC, Sweeney LG, Finlay WH (2009). Aerodynamic forces and moment on a sphere or cylinder attached to a wall in a Blasius boundary layer. Eng. App. Comp. Fluid Mech 3: 289–295.

[37]. Goldman AJ, Cox RG, Brenner H (1967). Slow viscous motion of a sphere parallel to a plane wall: I. Motion through a quiescent fluid. Chem. Eng. Sci 22: 637.

[38]. Goldman AJ, Cox RG, Brenner H (1967). Slow viscous motion of a sphere parallel to a plane wall: II. Couette flow. Chem. Eng. Sci 22: 653–660.

[39]. Bagnold RA (1974). Fluid forces on a body in shear flow; experimental use of stationary flow. Proc. Roy. Soc. London A 340: 147–171.

[40]. King MR & Leighton DT Jr (1997). Measurement of the inertial lift on a moving sphere in contact with a plane wall in a shear flow. Phys. Fluids, 9: 1248–1255.

[41]. Dandy DS & Dwyer HA (1990). A sphere in shear flow at finite Reynolds number: effect of shear on particle lift, drag, and heat transfer. J. Fluid Mech, 216: 381–410.

[42]. Burdick GM, Berman NS, Beaudoin SP (2001). Describing hydrodynamic particle removal from surfaces using the particle Reynolds number. J. Nanoparticle Res, 3: 453–465.

[43]. Muthanna C, Nieuwstadt FTM, Hunt JCR (2005). Measurement of the aerodynamic forces on a small particle attached to a wall. Exp. Fluids, 39: 455–463.

[44]. Hall D (1988). Measurement of the mean force on a particle near a boundary in turbulent flow. J. Fluid Mech 187: 451.

[45]. Mollinger AM & Nieuwstadt FTM (1996). Measurement of the lift force on a particle fixed to the wall in the viscous sublayer of a fully developed turbulent boundary layer. J. Fluid Mech, 316: 285–306.

[46]. Segre G & Silberberg A (1961). Radial particle displacements in Poiseuille flow of suspensions. Nature 189: 209–210.

[47]. Segre G & Silberberg A (1962). Behavior of macroscopic rigid spheres in Poiseuille flow I, II. Fluid Mech. 14: 115–135, 136–157.

[48]. Masironi LA & Fish BR (1964). Direct observation of particle reentrainment from surfaces in *Surface Contamination*, ed. by Fish BR (Oxford: Pergamon), pages 55–59.

[49]. Cox RG & Brenner H (1968). The lateral migration of solid particles in Poiseuille flow: I. Theory. Chem. Eng. Sci 23: 147–173.

[50]. Ho BP & Leal RG (1976). Inertial migration of rigid spheres in two-dimensional unidirectional flows. J. Fluid Mech 65: 365–400.

[51]. Cox RG & Hsu SK (1977). The lateral motion of solid particles in a laminar flow near a plane. Int. J. Multiphase Flow 3: 201–222.

[52]. Reeks MW, Reed J, Hall D (1988). On the resuspension of small particles by a turbulent flow. J. Phys. D 21: 574–589.

[53]. Schonberg JA & Hinch EJ (1989). The inertial migration of a sphere in Poiseuille flow. J. Fluid Mech 203: 517–524.

[54]. McLaughlin JB (1991). Inertial migration of a small sphere in linear shear flows. J. Fluid Mech, 224: 261–274.

[55]. Ziskind G, Fichman M, Gutfinger C (1997). Adhesion moment model for estimating particle detachment from a surface. J. Aerosol Sci, 28: 623–634.

[56]. Ziskind G, Fichman M, Gutfinger C (1998). Effects of shear on particle motion near a surface—application to resuspension. J. Aerosol Sci 29: 323–338.

[57]. Zhang F,Reeks M, Kissane M (2013). Particle resuspension in turbulent boundary layers and the influence of non-Gaussian removal forces. J. Aerosol Sci 58: 103–128.

[58]. Taneda J (1956). Experimental investigation of the wake behind a sphere at low Reynolds number. J. Phys. Soc. Jpn 11: 1104–1108.

[59]. Magarvey R & Bishop RL (1961). Transition ranges for three-dimensional wakes. Can. J. Phys 39: 1418–1422.

[60]. Orszag S, Tomboulides AG, Karniadakis GE (1993). Direct and large eddy simulations of axisymmetric wakes. AIAA paper, p. 546.

[61]. Johnson TA & Patel VC (1999). Flow past a sphere up to a Reynolds number of 300. J. Fluid Mech 378: 19–70.

[62]. Przadka W, Miedzik J, Gumowski K, Goujon-Durand S, Wesfreid W (2008). The wake behind the sphere: analysis of vortices during transition from steadiness to unsteadiness. Arch. Mech 60: 467–474.

[63]. Savory E & Toy N (1986). Hemispheres and hemisphere-cylinders in turbulent boundary layers. J. Wind Eng. Indust. Aerodynamics 23: 345–364.

[64]. Savory E & Toy N (1986). The flow regime in the turbulent near wake of a hemisphere. Exp. Fluids 4: 181–188.

[65]. Fedrizzi M, Giacobello M, Soria J, Atkinson C, Jones M (2012). Experimental investigation of a hemisphere in a thin flat plate boundary layer. Proceedings 18th Australasian Fluid Mechanics Conference (3–7 December 2012, Launceston, Australia).

[66]. Wood JN, De Nayer G, Schmidt S, Breuer M (2016). Experimental investigation and large-eddy simulation of the turbulent flow past a smooth and rigid hemisphere. Flow, Turbulence and Combustion 97 (1): 79–119.

[67]. Ledda PG, Siconolfi L, Viola F, Gallaire F, Camarri S (2018). Suppression of von Karman vortex streets past porous rectangular cylinders. Phys. Rev. Fluids, 3: 103901.

[68]. Patankar SV & Spalding DB (1972). A calculation procedure for heat, mass and momentum transfer in three-dimensional parabolic flows. Int. J. Heat Mass Transfer 15: 1789–1806.

[69]. Celik IB, Ghia U, Roache PJ (2008). Procedure for estimation and reporting of uncertainty due to discretization in {CFD} applications. J. Fluids {Eng. Trans. ASME}, 130(7).

[70]. Schlichting H (1979). Boundary-Layer Theory, 7th edition (New York: McGraw-Hill), tr. by Kestin J from the German *Grenzschlicht-Theorie* (Karlsruhe: Braun, 1951).

[71]. Jones R, Pollock HM, Cleaver JAS, Hodges CS (2002) Adhesion forces between glass and silicon surfaces in air studied by AFM: effects of relative humidity particle size, roughness, and surface treatment. Langmuir 18: 8045–8055.

[72]. Wanka S, Kappl M, Wolkenhauer M, Butt H-J (2013). Measuring adhesion forces in powder collectives by inertial detachment. Langmuir 29: 16075–16083. [PubMed: 24320051]

[73]. Cheng W, Dunn PF, Brach RM (2002). Surface roughness effects on microparticle adhesion. J. Adhesion 78: 929–965.

[74]. Wu Y, Cliff ID, Russell AG (1992). Controlled wind tunnel experiments for particle bounce-off and resuspension Aerosol Sci. Technol 17: 245–262.

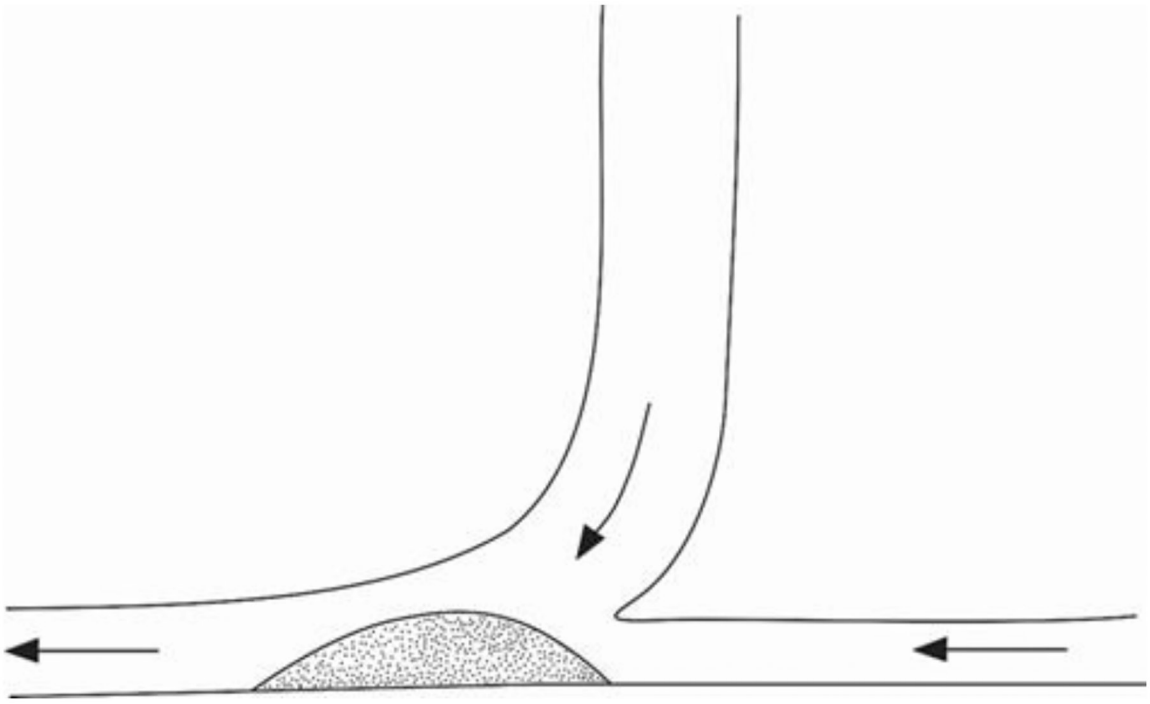

Figure 1.
Schematic of Entrance Tube into the Venturi Dustiness Tester.

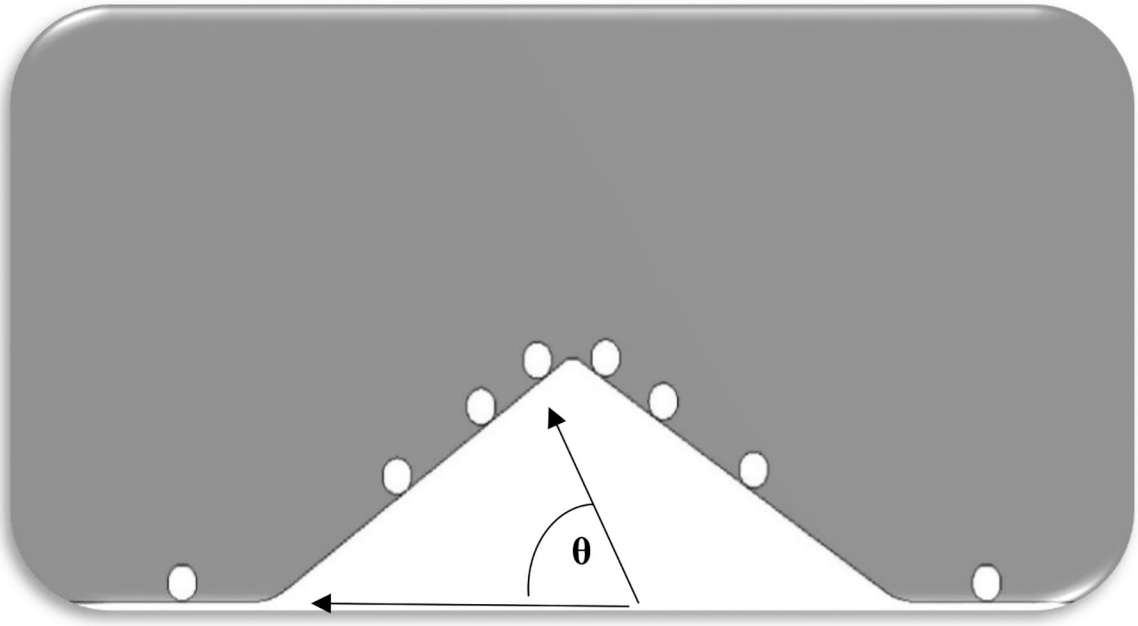

Figure 2.
Locations, θ, on the wedge. Fluid flow is left-to-right.

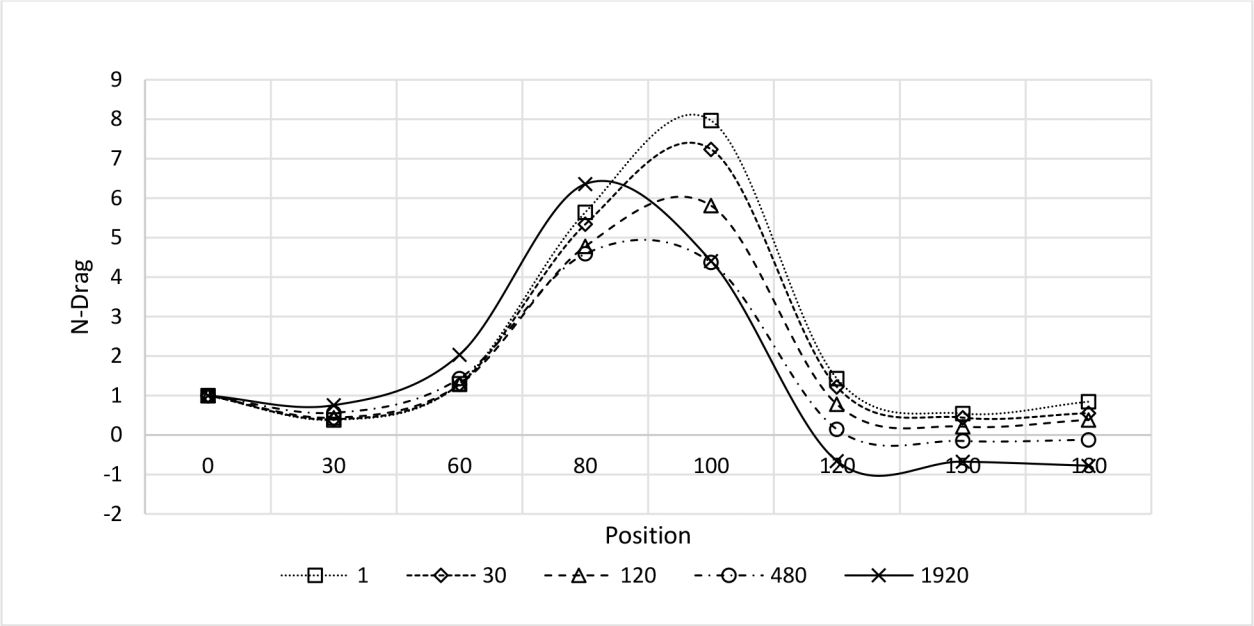

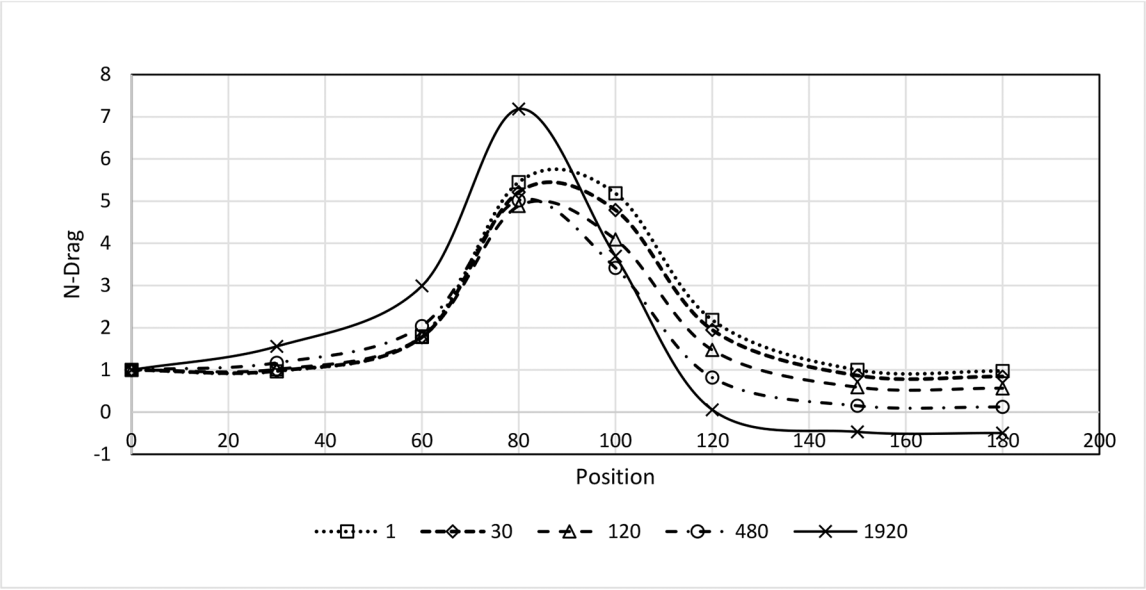

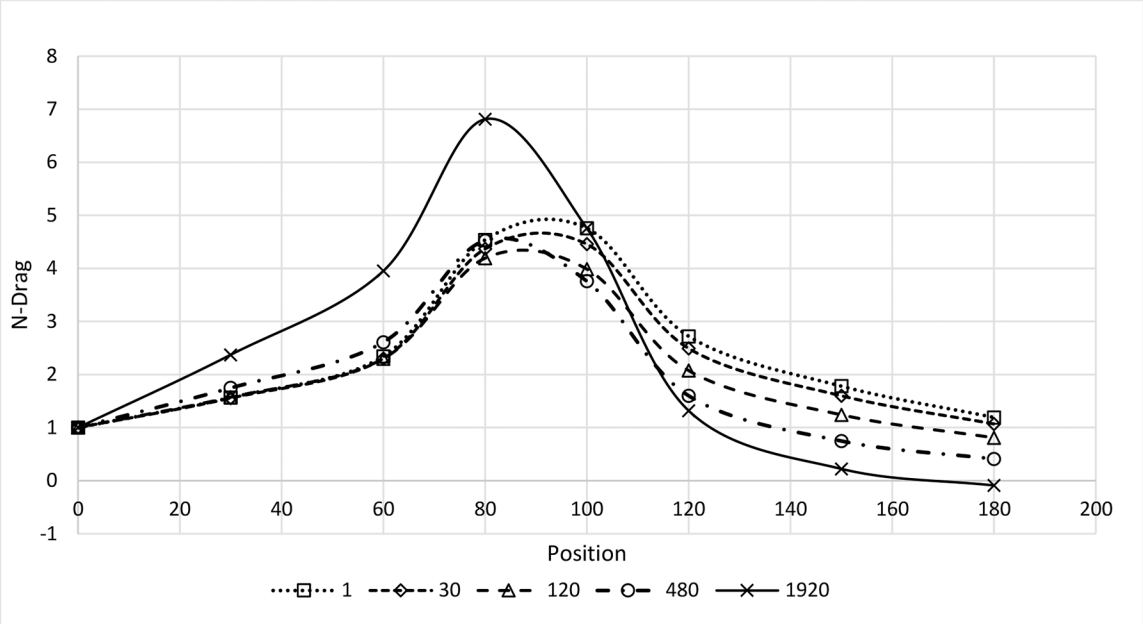

Figure 3.

Normalized drag $F_{drag}(\theta)/F_{drag}(0)$, for flow over a cylinder on a wedge with wedge angles α = 30° (a), α = 45° (b), α = 60° (c), for different $Re_{channel}$.

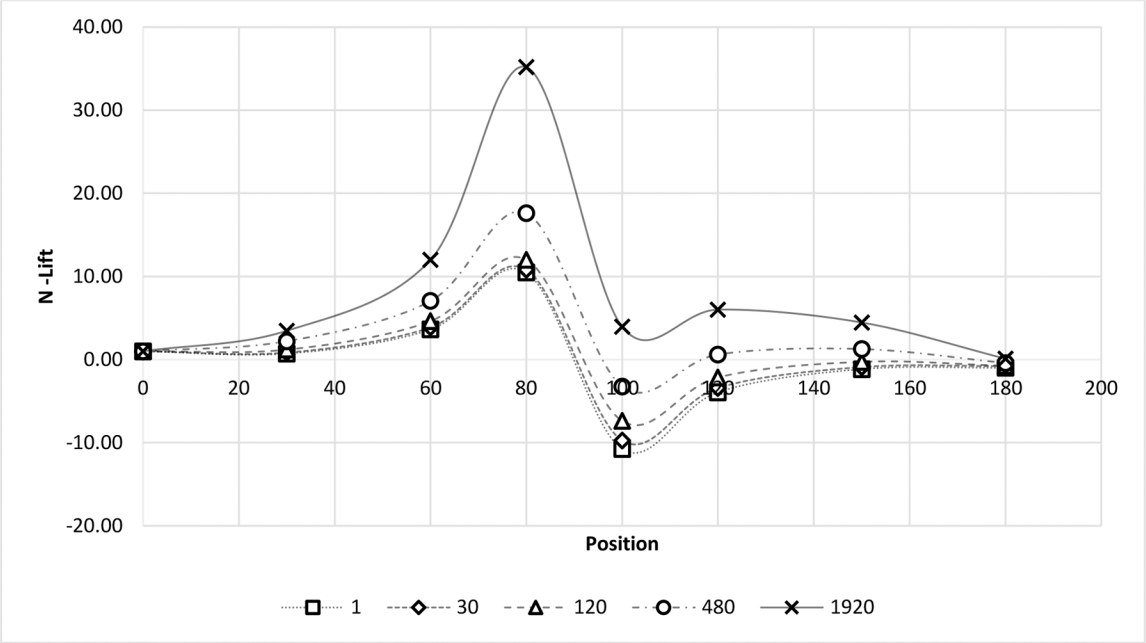

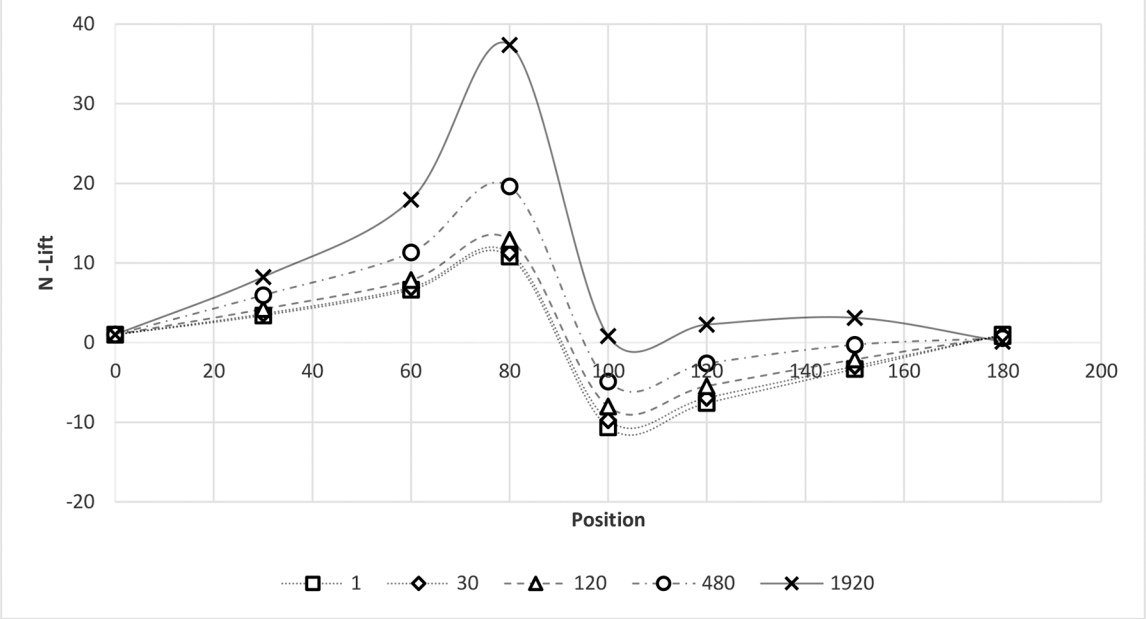

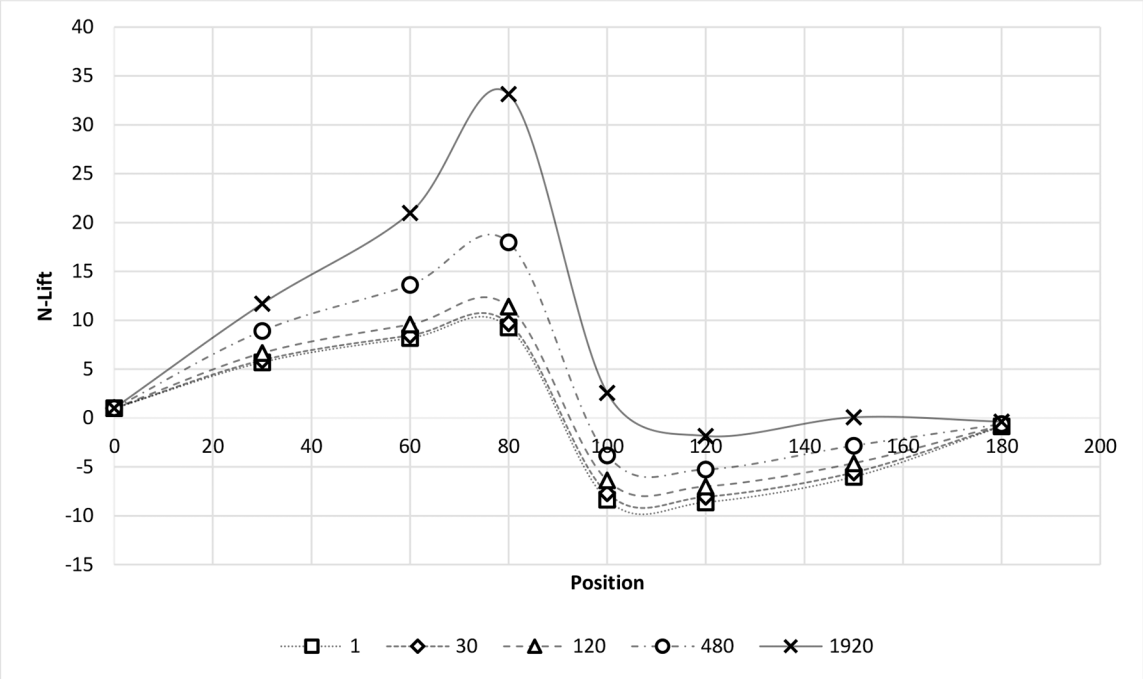

Figure 4.

Normalized lift, $F_{lift}(\theta)/F_{lift}(0)$, for flow over a cylinder on a wedge with wedge angle, α = 30° (a), α = 45° (b), α = 60° (c), for different $Re_{channel}$.

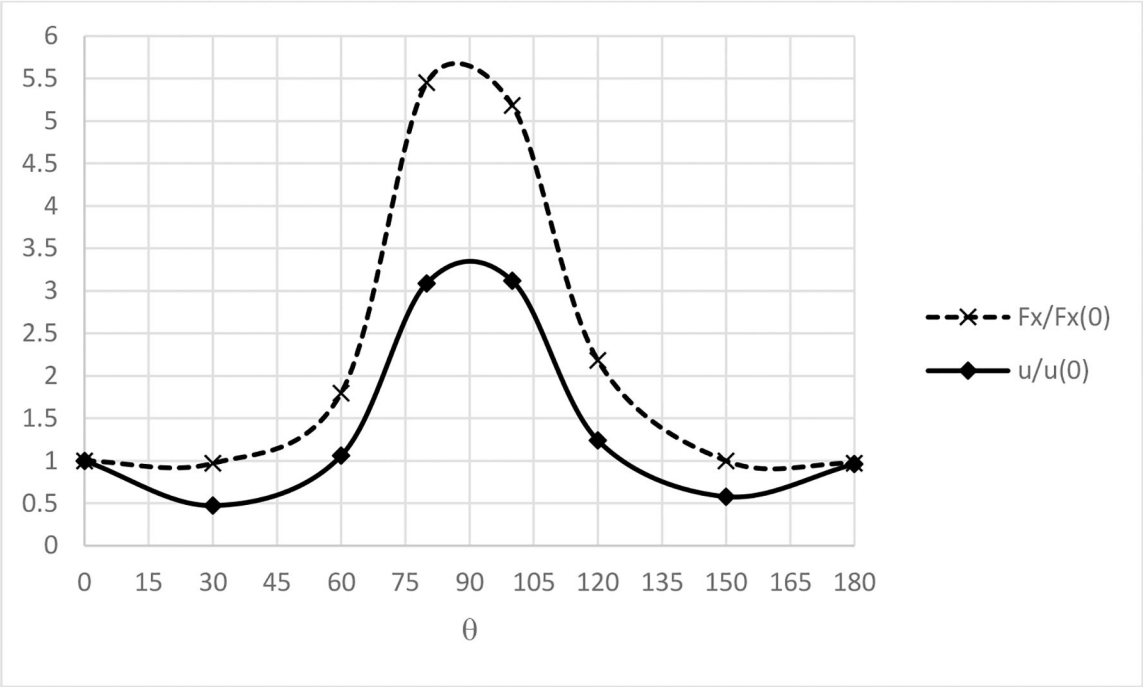

Figure 5.

Variation in the normalized force parallel to the unperturbed substrate $F_x(\theta)/F_x(0)$ (dashed line); variation in the normalized velocity parallel to the unperturbed substrate $u(\theta)/u(0)$ (solid line). Re = 1, wedge angle $\alpha = 45°$.

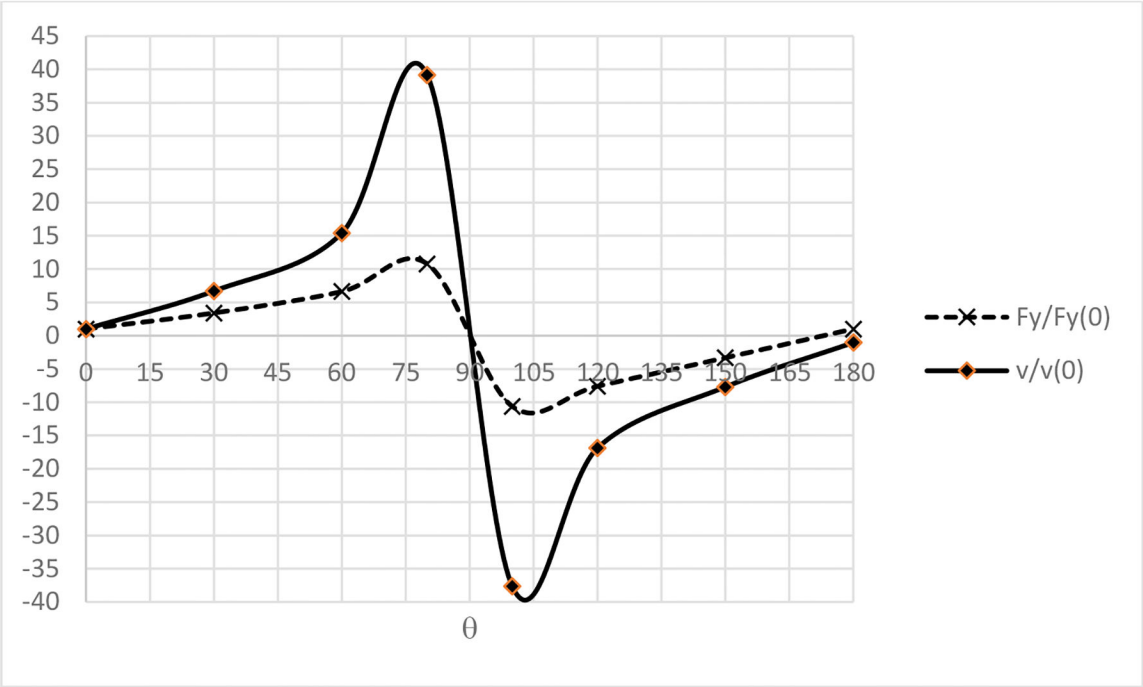

Figure 6.

Variation in the normalized force normal to the unperturbed substrate $F_y(\theta)/F_y(0)$ (dashed line); variation in the normalized velocity normal to the unperturbed substrate $v(\theta)/v(0)$ (solid line). Re = 1, wedge angle $\alpha = 45°$.

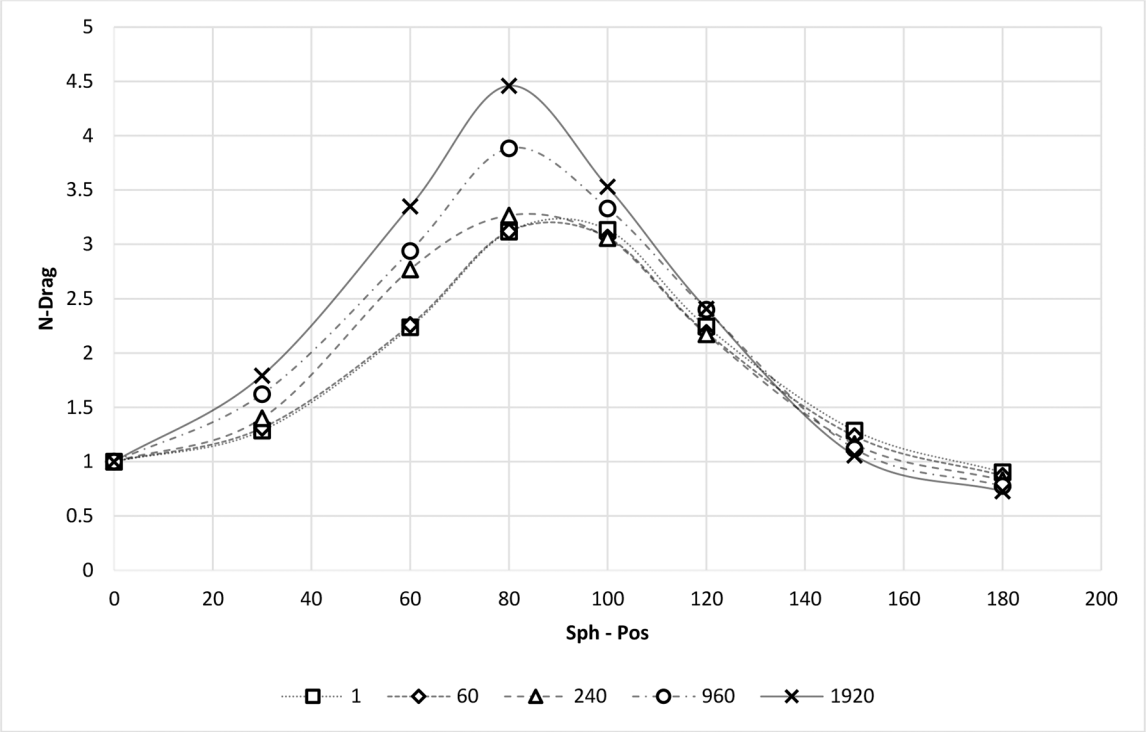

Figure 7.
Normalized drag for flow over a sphere on a cone with cone half angle $\alpha = 60°$ for different $Re_{channel}$

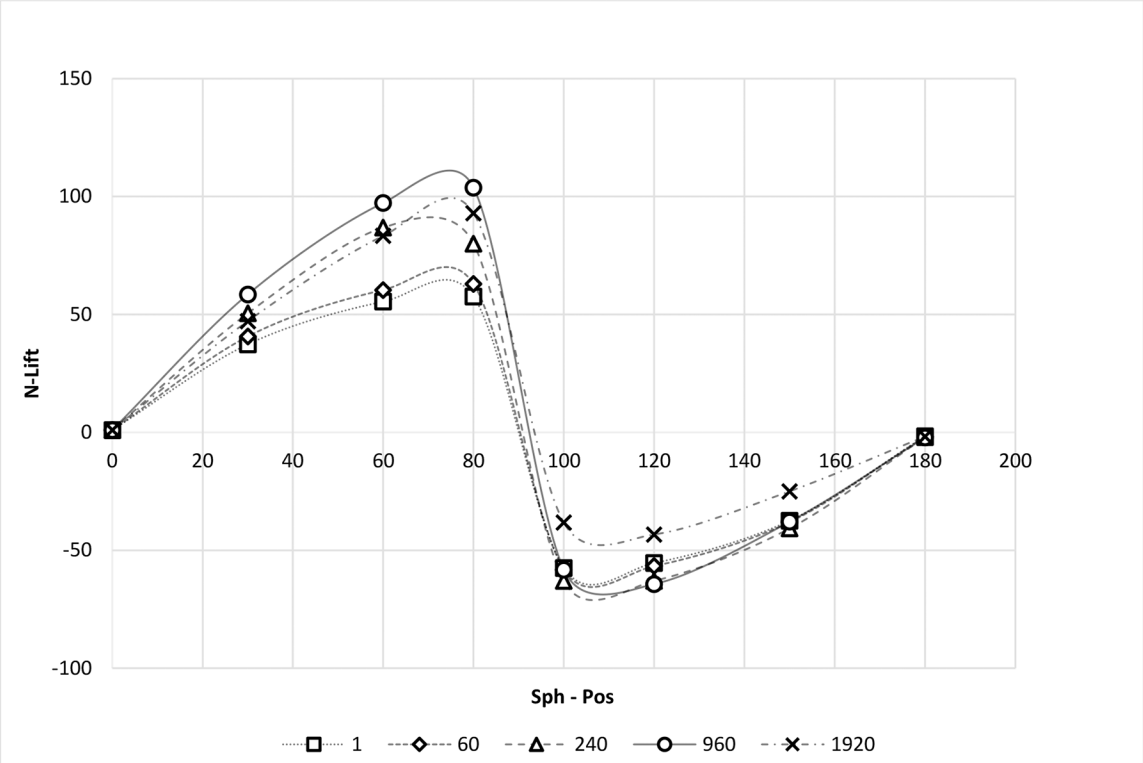

Figure 8.

Normalized lift for flow over a sphere on a cone with cone half angle α = 60° for different $Re_{channel}$

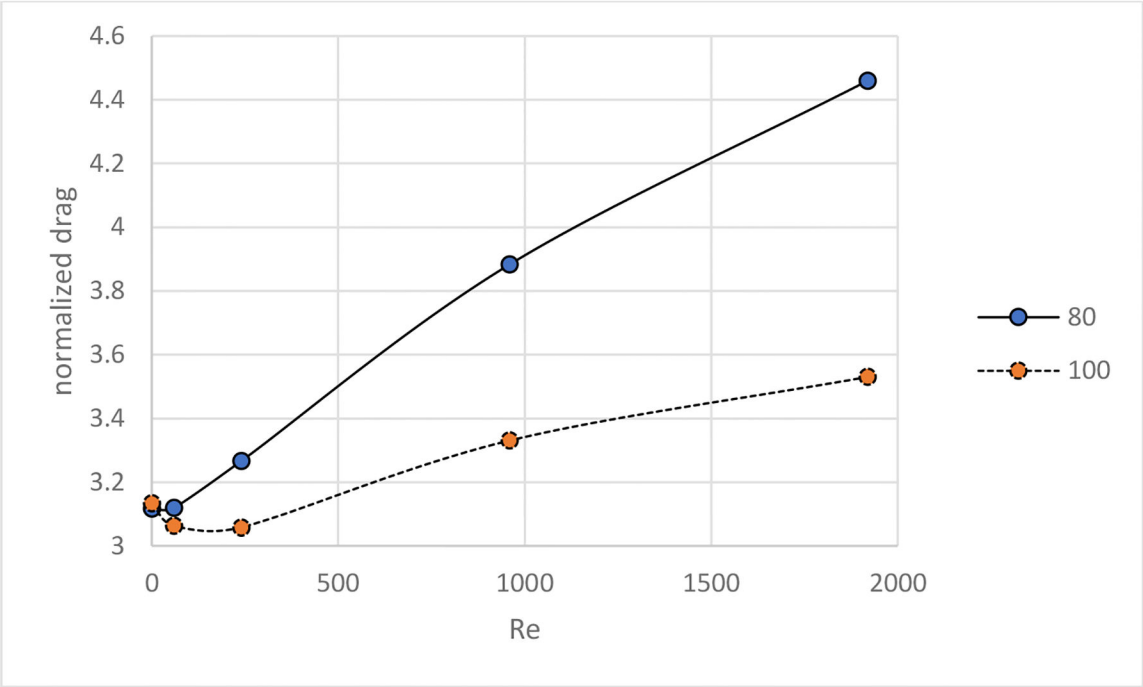

Figure 9.

Normalized drag for flow over a sphere near the summit (θ = 80°, 100°) of a cone with cone half angle α = 60° as a function of $Re_{channel}$

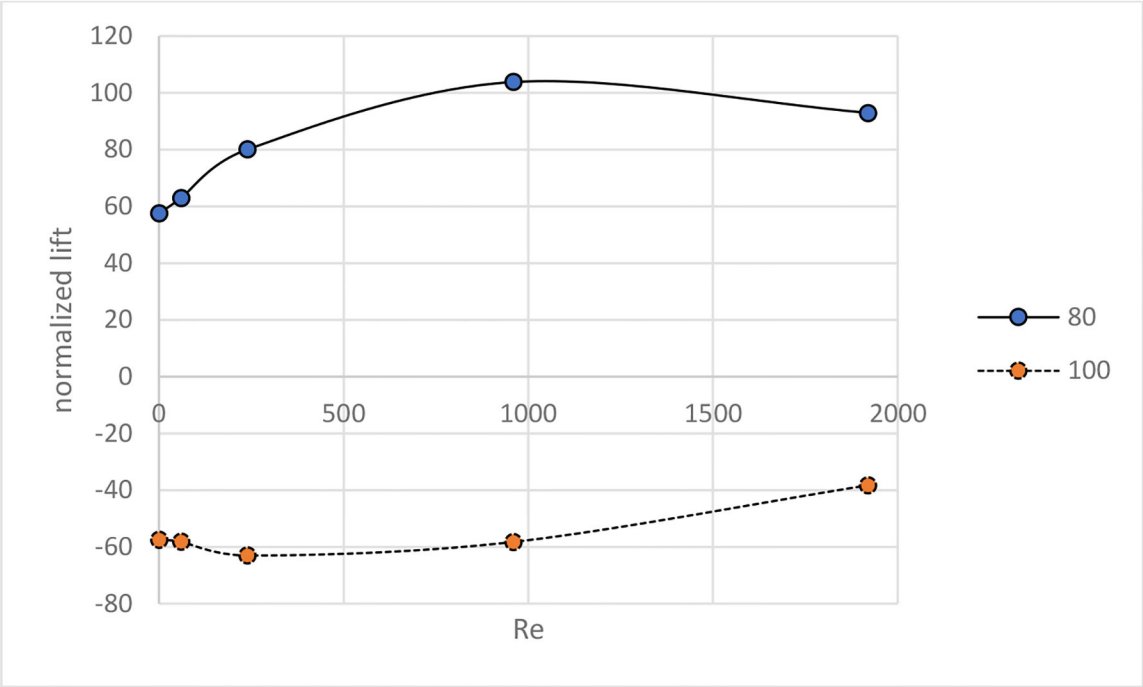

Figure 10.

Normalized lift for flow over a sphere near the summit (θ = 80°, 100°) of a cone with cone half angle α = 60° as a function of $Re_{channel}$

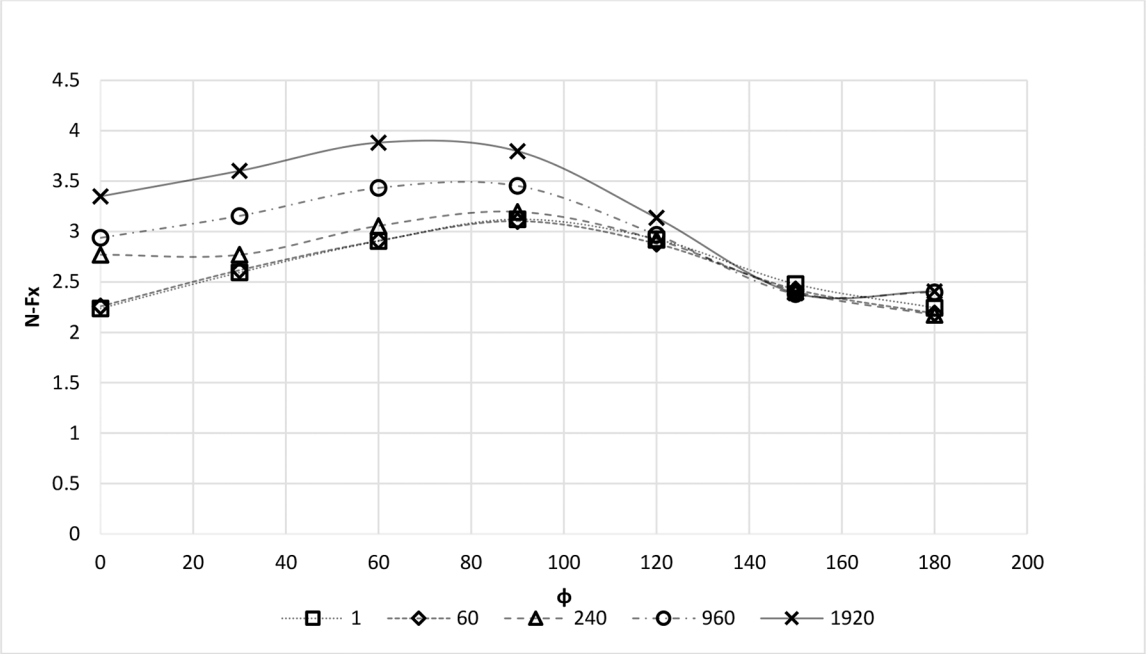

Figure 11.

Normalized drag for flow over a sphere at azimuthal locations on a cone with cone half angle $\alpha = 60°$ for different $Re_{channel}$

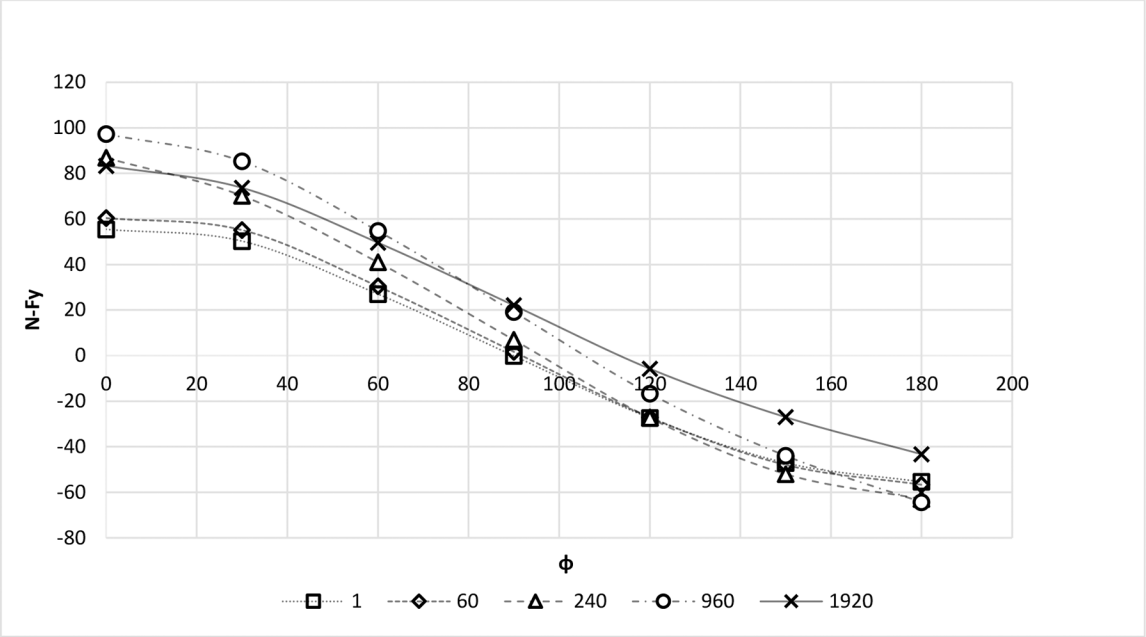

Figure 12.

Normalized lift for flow over a sphere at azimuthal locations on a cone with cone half angle $\alpha = 60°$ for different $Re_{channel}$

Table 1:

2D grid refinement results – Flow over a cylinder on a wedge

	No. of cells N	A/N [mm^2]	(A/N)$^{1/2}$ [mm]	r	Drag	% Difference	Lift	% Difference
Coarse	21672	3.7716	1.942		2.02984E-07		1.16822E-07	
Med	48800	1.6749	1.294	1.5	2.03285E-07	0.148	1.17489E-07	0.571
Fine	109800	0.74442	0.8628	1.5	2.03581E-07	0.146	1.18083E-07	0.506

Table 2:

3D grid refinement results – Flow over a sphere on a cone

	No. of Nodes N	V/N [mm^3]	V/N$^{1/3}$ [mm^3]	r	Drag Force [μdyne]	% Difference	Lift Force [μdyne]	% Difference
coarse	941077	16.338	2.5374		70.1492		22.3487	
medium	1935983	7.9417	1.9951	1.27	70.2165	0.096	22.4066	0.259
fine	7685427	2.0005	1.2600	1.58	69.6636	−0.692	22.3467	−0.009